# Rational Design of Carbon-Doped Carbon Nitride/$Bi_{12}O_{17}Cl_2$ Composites: A Promising Candidate Photocatalyst for Boosting Visible-Light-Driven Photocatalytic Degradation of Tetracycline

Chengyun Zhou,[†] Cui Lai,[†] Piao Xu,[†] Guangming Zeng,*[●] Danlian Huang,*[●] Zhihao Li, Chen Zhang, Min Cheng, Liang Hu, Jia Wan, Fei Chen, Weiping Xiong, and Rui Deng

College of Environmental Science and Engineering, Hunan University and Key Laboratory of Environmental Biology and Pollution Control (Hunan University), Ministry of Education, 8 South Lushan Road, Yuelu District, Changsha 410082, P. R. China

S Supporting Information

**ABSTRACT:** Many recent advances based on 2D materials have opened new possibilities in photocatalysis. In this paper, a new 2D semiconductor composite consisting of carbon-doped carbon nitride (denoted as CCN) layers and $Bi_{12}O_{17}Cl_2$ layers was designed via an *in situ* method. A supramolecular chemistry approach was employed to form CCN by using the hydrogen-bonded melamine−cyanuric acid and barbituric acid, and $Bi_{12}O_{17}Cl_2$ layers were obtained by using a moderate solvothermal method. $CCN/Bi_{12}O_{17}Cl_2$ composite had superior photocatalytic performance for degrading antibiotic tetracycline (TC) under visible-light irradiation. The degradation rate constant of $20\%CCN/Bi_{12}O_{17}Cl_2$ is 0.0409 $min^{-1}$, which is approximately 2.9-, 1.5-, and 32.1-fold those of pristine $Bi_{12}O_{17}Cl_2$, CCN, and BiOCl, respectively. Electrochemical measurements showed that $CCN/Bi_{12}O_{17}Cl_2$ composite has high photogenerated charge carrier separation efficiency. According to the trapping and electron spin resonance results, superoxide radicals and holes were the main active radicals in the degradation of TC. The enhanced photocatalytic activity of $CCN/Bi_{12}O_{17}Cl_2$ can be attributed to enhanced charge separation. It is expected that the $CCN/Bi_{12}O_{17}Cl_2$ composite could be utilized as visible-light photocatalyst for other environmental applications.



**KEYWORDS:** *Carbon-doped carbon nitride, $Bi_{12}O_{17}Cl_2$, Semiconductor composites, Visible-light photocatalysis, Antibiotic degradation*
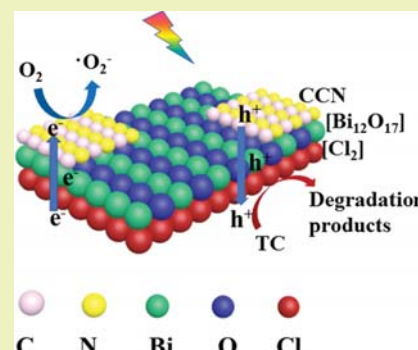
## ■ INTRODUCTION

In recent decades, the rapid development of society has caused some problems like energy shortage and environmental deterioration.[1−5] The emerging environmental contaminants such as phenols, pesticides, and antibiotics in water cycling systems, especially in drinking water, have posed serious threats to organisms and human beings' health even at low levels.[6−10] The American Environment Protection Agency has listed them as priority control contaminants.[11−15] Many effective treatments have been developed to address these serious issues, including biological treatment,[16,17] adsorption,[18−23] photocatalysis,[24] and so on. Biological degradation has proven to be a promising method for the degradation of organics since organics can transform into inorganic molecules via some specific bacteria.[25−27] Nonetheless, biological remediation requires a relatively long period of time.[28,29] Different from this, photocatalytic degradation technology could utilize solar energy to achieve the mineralization of contaminated organics.

The semiconductor photocatalyst has great potential in resolving environmental problems caused by organic pollutants.[7,30] To realizing this target, the key point is to search for the appropriate photocatalysts with sufficient sunlight absorption and efficient photoinduced charge separation.[31,32] Because of its layer structure, and high chemical and optical stability, the

ternary semiconductor bismuth oxychloride (BiOCl) has attracted extensive attention.[33] BiOCl could not utilize visible light, but it could construct the desired band-gap semiconductors where the band gap can be adjusted by the ratio of Cl and O, such as $Bi_{12}O_{17}Cl_2$. $Bi_{12}O_{17}Cl_2$ has a unique layered structure, excellent photophysical and chemical properties. Also, this material is nontoxic and chemically stable. These fascinating properties have attracted a great deal of research interest and can be applied to environmental remediation.[34] It has been employed to oxidize benzyl alcohol and degrade bisphenol A under visible light.[35,36] A number of $Bi_{12}O_{17}Cl_2$-based composite photocatalysts have been synthesized, such as $BiOI@Bi_{12}O_{17}Cl_2$,[37] $Bi_{12}O_{17}Cl_2/\beta$-$Bi_2O_3$,[38] and BiOCl-$Bi_{12}O_{17}Cl_2$.[39] Nevertheless, $Bi_{12}O_{17}Cl_2$ composited with nonmetal photocatalysts has not been achieved. In addition, as reported by Zhang et al., the internal electric field between $(Bi_{12}O_{17})$ and $(Cl_2)$ drives the electrons from $Bi_{12}O_{17}Cl_2$, which are further transferred to other semiconductors.[40] This hypothesis is good for us to build an efficient photocatalysis system.

Graphitic carbon nitride ($g$-$C_3N_4$) with a conjugated system attracts tremendous scientific interest for water splitting, $CO_2$ oxidation, and contaminant degradation.[41−43] Wang et al. prepared $g$-$C_3N_4$ and applied it for water splitting under visible light.[44] Many researchers have utilized $g$-$C_3N_4$ in contaminant degradation.[45] However, the low quantum efficiency, ultrafast recombination of photoinduced charge carriers, and insufficient sunlight absorption currently have limited the practical application of $g$-$C_3N_4$.[46−49] Fortunately, these shortcomings might be overcome through composition with other photocatalysts, such as $TiO_2$,[50] $ZnO$,[24] $Bi_2WO_6$,[51−53] and $BiVO_4$.[54−58] Motivated by flourishing studies on composite photocatalysts, we focused this work on the contact between $g$-$C_3N_4$ and $Bi_{12}O_{17}Cl_2$ due to the good absorption properties of $g$-$C_3N_4$ and good electrical conductivity of the $Bi_{12}O_{17}Cl_2$ layer.

Herein, the $Bi_{12}O_{17}Cl_2$-hybridized carbon-doped $g$-$C_3N_4$ (denoted as CCN) composites with different proportions were fabricated in this study. The microstructure, optical properties, and photoelectric performances of CCN/$Bi_{12}O_{17}Cl_2$ were investigated. The degradation kinetics of the prepared photocatalyst on common antibiotic pollutants (i.e., tetracycline) was explored under visible light. It is fascinating to find that CCN/$Bi_{12}O_{17}Cl_2$ exhibits outstanding photocatalytic activity toward degradation of tetracycline (TC) compared with pristine $Bi_{12}O_{17}Cl_2$. The band-gap structure and proposed mechanism were proposed.

## EXPERIMENTAL SECTION

**Preparation of Catalysts.** The synthesized procedure of CCN was in accordance to our previous report.[59] The CCN samples were prepared by using melamine (1 mmol), cyanuric acid (1 mmol), and barbituric acid (0.1 mmol) in 80 mL of ethanol. Then, the mixture was sonication for 1 h and stirred for another 2 h. The mixture was dried in 80 °C. The dried product was calcined at 550 °C for 4 h at a heating rate of 3.6 °C min$^{-1}$. The obtained powder was centrifuged, washed, and dried. Then, the yellow resultant carbon-doped carbon nitride (CCN) was obtained. The typical bulk carbon nitride (CN) was obtained by merely using melamine.

$Bi_{12}O_{17}Cl_2$ was prepared by a solvothermal method.[60,61] $Bi(NO_3)_3$· $5H_2O$ (2.5 mmol) was dissolved in ethylene glycol (10 mL). Then, the mixture was added into 60 mL of distilled water containing 6 mmol of $NH_4Cl$ and 20 mmol of NaOH. The mixture was heated at 160 °C for 12 h. The resulting product was collected, washed with distilled water and ethanol, and dried.

The CCN/$Bi_{12}O_{17}Cl_2$ composite was prepared by an *in situ* method. First, the as-prepared sample was dispersed into methanol (100 mL), and kept under ultrasonic conditions for 1 h to promote the dispersion of CCN. Then, a given mass of $Bi_{12}O_{17}Cl_2$ was added into the above mixture, under sonication for another 1 h. After that, the mixture was stirred for 12 h. Then, the mixture was separated and washed. The sample was dried and further treated at 120 °C for 2 h in air to enhance the interaction between $Bi_{12}O_{17}Cl_2$ and the carbon nitride matrix. The samples were labeled X CCN/$Bi_{12}O_{17}Cl_2$ (X is the mass ratio of CCN to samples). They were 5% CCN/$Bi_{12}O_{17}Cl_2$, 10% CCN/$Bi_{12}O_{17}Cl_2$, 20% CCN/$Bi_{12}O_{17}Cl_2$, and 30% CCN/$Bi_{12}O_{17}Cl_2$.

**Characterization Methods.** The structure of samples was obtained by scanning electron microscopy (SEM; FEI, Helios NanoLab 600i dual beam system) and transmission electron microscopy (HAADF STEM; Tecnai G2F20). X-ray diffraction data was obtained by a Rigaku diffractometer. XPS data was obtained by an ESCALAB 250Xi spectrometer (Thermo Fisher). The UV−vis diffuse reflectance spectra (DRS) were measured on a Cary 300 UV−vis spectrophotometer. Electron spin resonance (ESR) signals were collected on a Bruker ER200-SRC spectrometer.

**Photocatalytic Experiments.** The photocatalytic degradation activities were conducted by the degradation of TC. A 300 W Xe lamp with a 420 nm cutoff filter was used as the light source. The

degradation pollutants were 50 mL of TC aqueous solution (20 mg L$^{-1}$). The dosage of photocatalyst was 1 g L$^{-1}$. Before irradiation, the solution was stirred in the dark for 1 h to achieve a balance. Then, the solution was exposed to visible light. At a given time, 3 mL of solution was withdrawn and filtrated. The concentration of TC was determined by the UV−vis spectrophotometer, and the maximum peak was 357 nm.

**Electrochemical Measurements.** The electrochemical properties were realized in a CHI-660D workstation. The working electrode was fabricated on fluorine-doped tin oxide (FTO) glass. The Pt plate was utilized as the counter electrode and Ag/AgCl as the reference electrode. $Na_2SO_4$ solution (0.2 M) was used as the measure system aqueous electrolyte. The photocurrent responses of the samples were collected on 0 V. In addition, electrochemical impedance spectroscopy (EIS) and the Mott−Schottky test were also performed in this system.

## RESULTS AND DISCUSSION

**Catalysts Characterization.** The morphology and compositions of $Bi_{12}O_{17}Cl_2$, CCN, and CCN/$Bi_{12}O_{17}Cl_2$ were determined by SEM with the energy-dispersive spectrometry (EDS) analysis. As shown in Figure 1a, $Bi_{12}O_{17}Cl_2$ possessed a
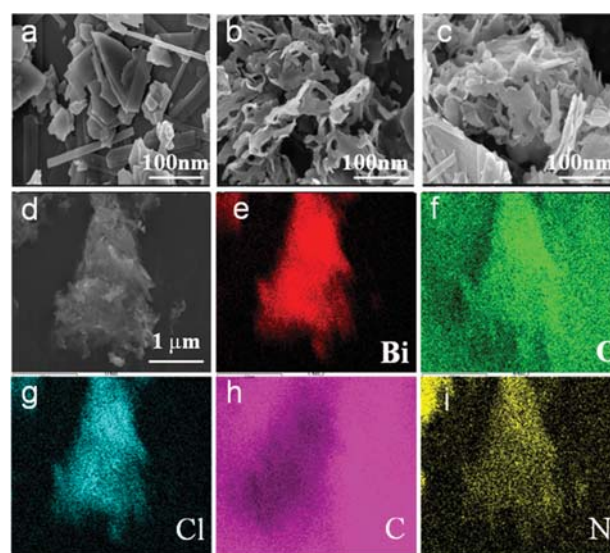


**Figure 1.** SEM images of samples $Bi_{12}O_{17}Cl_2$ (a), CCN (b), and CCN/$Bi_{12}O_{17}Cl_2$ (c, d). (e−i) Corresponding elemental maps of CCN/$Bi_{12}O_{17}Cl_2$.

nanosheet structure. The CCN exhibited nanosheets with stacked layers and smooth surface in Figure 1b. In Figure 1c,d, the CCN nanosheet integrates with the 2D $Bi_{12}O_{17}Cl_2$ nanosheet effectively, which may pose a large effect on the photocatalytic activity. Meanwhile, the EDS mappings were utilized to identify the elements of CCN/$Bi_{12}O_{17}Cl_2$ in Figure 1e−i. The elements are distributed on the surface, suggesting that the CCN/$Bi_{12}O_{17}Cl_2$ is composed of CCN and $Bi_{12}O_{17}Cl_2$ components. Further detailed morphology and crystallography of the samples were studied by TEM in Figure 2. The layered structure of CCN (Figure 2a) and the nanosheet structure of $Bi_{12}O_{17}Cl_2$ (Figure 2b) were found. The length and width of the $Bi_{12}O_{17}Cl_2$ nanosheet were 200−400 and 40−100 nm, respectively. The $Bi_{12}O_{17}Cl_2$ nanosheets disperse on the surface of CCN uniformly, which would effectively enhance the interaction between them (Figure 2c). The CCN/$Bi_{12}O_{17}Cl_2$ was further studied by HRTEM in Figure 2d. It was observed that the lattice distance was 0.338 nm, corresponding to the
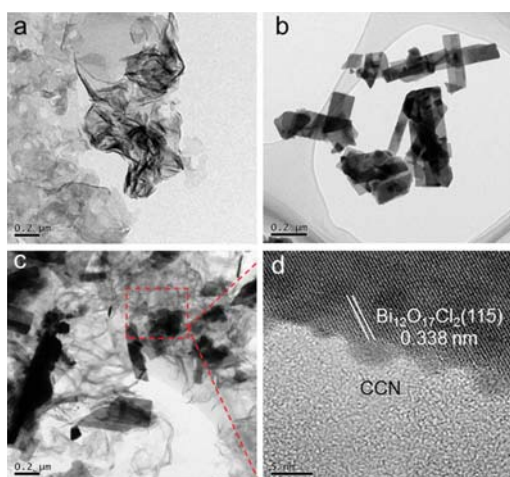
**Figure 2.** TEM images of CCN (a), $Bi_{12}O_{17}Cl_2$ (b), and CCN/$Bi_{12}O_{17}Cl_2$ (c). (d) HRTEM images of CCN/$Bi_{12}O_{17}Cl_2$.

(115) facets of $B_{12}O_{17}Cl_2$. The CCN nanosheets were employed as the substrate of $B_{12}O_{17}Cl_2$, and marked in Figure 2c,d. The interaction of $B_{12}O_{17}Cl_2$ and CCN enhances the separation efficiency of photocarriers.

The crystal structures and phase purity of pristine CCN, $Bi_{12}O_{17}Cl_2$, and all the CCN/$Bi_{12}O_{17}Cl_2$ samples were determined by XRD. The peaks of CCN located at 13.1° and 27.2° were indexed as (100) and (002), respectively (Figure 3a). The (002) peak of CCN obviously became weaker and
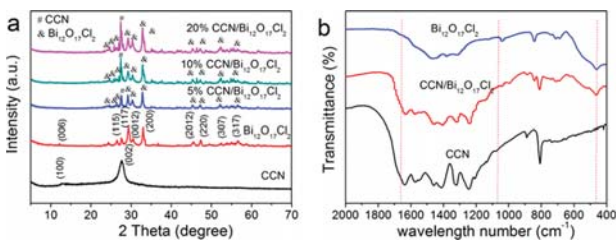


**Figure 3.** (a) XRD patterns of samples CCN, $Bi_{12}O_{17}Cl_2$, and CCN/$Bi_{12}O_{17}Cl_2$ (5%, 10%, and 20%). (b) FT-IR Spectra of samples CCN, $Bi_{12}O_{17}Cl_2$, and CCN/$Bi_{12}O_{17}Cl_2$.

broader compared to the bulk CN (in Figure S1), indicating the reduced layer thickness.[62] The main peaks of $Bi_{12}O_{17}Cl_2$ at 24.57°, 29.46°, and 32.97° could be ascribed to (115), (117), and (200) of $Bi_{12}O_{17}Cl_2$ (JCPDS 37-0702), respectively.[60] With the increased CCN content, the intensity of (002) was enhanced in the CCN/$Bi_{12}O_{17}Cl_2$. These results indicated that the CCN/$Bi_{12}O_{17}Cl_2$ samples were successful obtained.

Figure 3b shows the spectra of CCN, $Bi_{12}O_{17}Cl_2$, and CCN/$Bi_{12}O_{17}Cl_2$ composite. Signals in the 400−600 regions can be attributed to Bi—O units stretching in $Bi_{12}O_{17}Cl_2$. The bending modes C—N bond of CCN was at 810 cm$^{-1}$. The band in 1200−1600 cm$^{-1}$ can be attributed to the stretching of aromatic C—N. Signals at 1632 cm$^{-1}$ were related to the stretching vibration of C=N.[63] All the characteristic absorption peaks of $Bi_{12}O_{17}Cl_2$ and CCN were observed in the CCN/$Bi_{12}O_{17}Cl_2$ composite, indicating that $Bi_{12}O_{17}Cl_2$ successfully composited with CCN, which was consistent with XRD results.

The surface elemental compositions and binding state of CCN/$Bi_{12}O_{17}Cl_2$ composite were evaluated by XPS analyses in

Figure 4. Elements were detected in the spectrum of CCN/$Bi_{12}O_{17}Cl_2$ (Figure 4a). Peaks at 164.3 and 158.9 eV refer to Bi
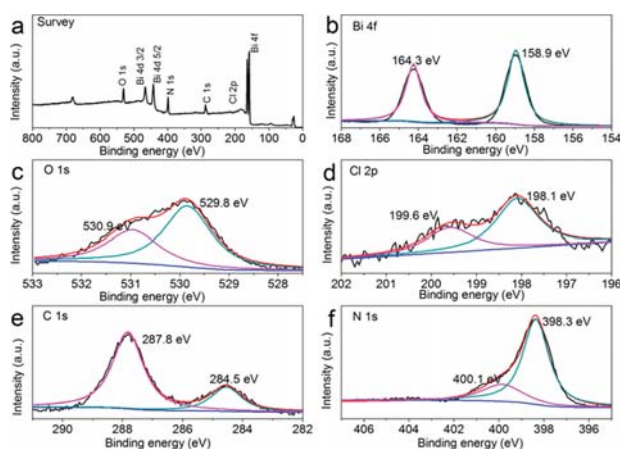


**Figure 4.** XPS spectra of CCN/$Bi_{12}O_{17}Cl_2$ survey spectra (a), high-resolution Bi 4f (b), high-resolution O 1s (c), high-resolution Cl 2p (d), high-resolution C 1s (e), and high-resolution N 1s (f).

$4f_{5/2}$ and Bi $4f_{7/2}$, respectively, which indicated that the $Bi^{3+}$ species was in CCN/$Bi_{12}O_{17}Cl_2$ (Figure 4b). The Cl 2p peak can be separated into 199.6 and 198.1 eV, respectively (Figure 4c). For the O 1s peak, it can be separated into two peaks. The peak located at 530.9 eV may belong to the O—H bond absorbed on the surface, and another peak at 529.8 eV may result from the lattice Bi—O—Bi bond (Figure 4d). In Figure 4e, the peaks of C 1s at 287.8 and 284.5 eV are found, which correspond to N=C—N bonding and C—C bonding, respectively. The N 1s peak divides into two peaks, which were located at 398.4 and 400.1 eV (Figure 4f). The binding at 398.4 eV was due to the triazine rings (C=N—C), and 400.1 eV was attributed to the tertiary nitrogen (N—C$_3$).[60] Additionally, the XPS of bulk CN, CCN, and $Bi_{12}O_{17}Cl_2$ is shown in Figure S2. The carbon doping effect and composition change have been confirmed by organic elemental analysis (OEA). The carbon content in as-prepared samples increased from 35.48% to 37.96% corresponding to the samples from CN to CCN (Table 1). The quantity of carbon doping was about

**Table 1. Results of Organic Elemental Analyses for CN and CCN**

| sample | C/% | H/% | N/% | C/N |
|--------|------|------|-------|------|
| CN | 35.48 | 2.32 | 62.20 | 0.57 |
| CCN | 37.96 | 1.85 | 60.19 | 0.63 |

2.48%. The molar ratio of C/N increased from 0.57 in CN to 0.63 in CCN. Results show that carbon was incorporated into CN successfully. In addition, the molar ratios of C/N by XPS spectra were also presented (Table S1). The changes of C/N molar ratio are also obtained after carbon doping, which is consistent with the result of OEA.

**Optical Properties and Electrochemical Analysis.** DRS spectra of $Bi_{12}O_{17}Cl_2$, CCN, and CCN/$Bi_{12}O_{17}Cl_2$ composites were presented (Figure 5a). The $Bi_{12}O_{17}Cl_2$ has an absorption edge at about 520 nm and, meanwhile, the CCN at about 560 nm.[50,64] The optical transitions of $Bi_{12}O_{17}Cl_2$ and CCN were indirect and direct, respectively.[36,65] The changes of $(\alpha h\nu)$ as a function of $(h\nu)$ are shown in Figure 5b. The band gaps of
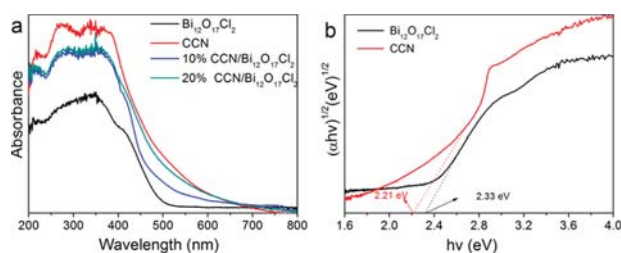
**Figure 5.** (a) UV−vis adsorption spectra of samples. (b) Plots of $(\alpha h\nu)^{1/2}$ vs photon energy $(h\nu)$ for $Bi_{12}O_{17}Cl_2$ and plots of $(\alpha h\nu)^2$ vs photon energy $(h\nu)$ for CCN.

$Bi_{12}O_{17}Cl_2$ and CCN were 2.33 and 2.21 eV, respectively. Compared with the original $Bi_{12}O_{17}Cl_2$, the $CCN/Bi_{12}O_{17}Cl_2$ photocatalyst had an enhanced absorption as the amount of CCN increased.

The photocurrent response of the sample was used to certify the efficiency separation of photogenerated electron−hole pairs.[66] The photocurrent responses of CCN, $Bi_{12}O_{17}Cl_2$, and $CCN/Bi_{12}O_{17}Cl_2$ at light on and off were stable and reversible (Figure 6a). The photocurrent of $CCN/Bi_{12}O_{17}Cl_2$ was about
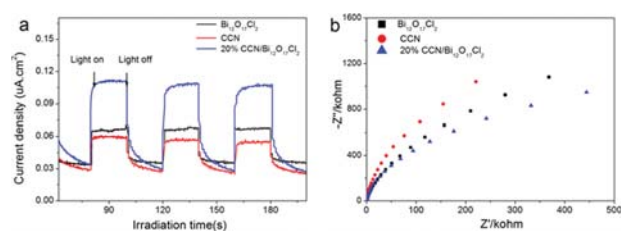


**Figure 6.** Photocurrent transient measurement (a) and electrochemical impedance spectra (b) of photocatalysts.

3-fold that of $Bi_{12}O_{17}Cl_2$. The separation efficiency of charge can be further investigated by EIS. A smaller arc radius in EIS represents more efficient charge separation. The EIS Nyquist plots of $Bi_{12}O_{17}Cl_2$ and $CCN/Bi_{12}O_{17}Cl_2$ are presented in Figure 6b. The radius of $CCN/Bi_{12}O_{17}Cl_2$ was smaller than that of $Bi_{12}O_{17}Cl_2$, which suggested that $CCN/Bi_{12}O_{17}Cl_2$ had a high efficiency of charges as compared to $Bi_{12}O_{17}Cl_2$. These results indicated that interaction existed in the interface of CCN and $Bi_{12}O_{17}Cl_2$, which is suitable for the separation of photogenerated carriers.

**Photocatalytic Activity.** The photocatalytic activities of $Bi_{12}O_{17}Cl_2$, CCN, and $CCN/Bi_{12}O_{17}Cl_2$ composites were measured for the degradation of TC. TC is a colorless and refractory pollutant. Figure 7a shows the degradation efficiency of TC under different times. The adsorption efficiency of
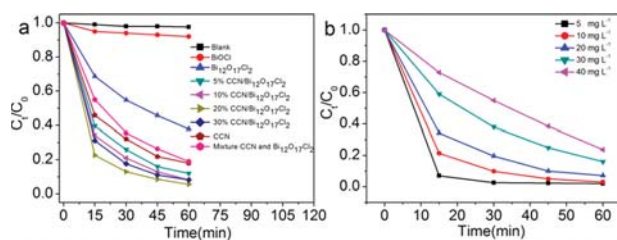


**Figure 7.** (a) Photodegradation rate of TC on different photocatalysts. (b) Effects of initial concentration of TC on $CCN/Bi_{12}O_{17}Cl_2$.

samples was investigated (Table S2). The degradation of TC aqueous solution was negligible without photocatalyst (Figure 7a). The removal of TC with BiOCl, $Bi_{12}O_{17}Cl_2$, and CCN in 1 h of irradiation was 8%, 54%, and 82%, respectively. All of $CCN/Bi_{12}O_{17}Cl_2$ composites showed superior degradation activities compared to the pristine CCN and $Bi_{12}O_{17}Cl_2$, which can be ascribed to the interaction of composites. When the content of CCN is 20%, the $CCN/Bi_{12}O_{17}Cl_2$ presented the highest photocatalytic activity with an efficiency of 94% in 1 h. However, excess CCN will act as the carriers' recombination center and hindered the light absorption of $Bi_{12}O_{17}Cl_2$. Therefore, the photocatalytic activity of 30% $CCN/Bi_{12}O_{17}Cl_2$ was decreased.

In addition, the mechanical mixture of CCN and $Bi_{12}O_{17}Cl_2$ with a 20% mass ratio showed lower photocatalytic activity than that of 20% $CCN/Bi_{12}O_{17}Cl_2$. As presented in Figure S3, all of the samples fit well with the pseudo-first-order model. Furthermore, the degradation rate for TC is shown in Table 2. The 20% $CCN/Bi_{12}O_{17}Cl_2$ composite displayed the fastest

**Table 2. Pseudo-First-Order Rate Constants ($K_{app}$) and Degradation Efficiencies for the TC in Different Photocatalytic Systems**

| sample | $K_{app}/min^{-1}$ | degradation efficiencies/% |
|---|---|---|
| BiOCl | 0.0013 | 8.1 |
| $Bi_{12}O_{17}Cl_2$ | 0.0157 | 62.2 |
| 5% $CCN/Bi_{12}O_{17}Cl_2$ | 0.0343 | 88 |
| 10% $CCN/Bi_{12}O_{17}Cl_2$ | 0.0397 | 91.8 |
| 20% $CCN/Bi_{12}O_{17}Cl_2$ | 0.0409 | 94 |
| 30% $CCN/Bi_{12}O_{17}Cl_2$ | 0.0402 | 91.8 |
| mixture | 0.027 | 81.9 |
| CCN | 0.0278 | 80.9 |

reaction rate in degradation of TC with the apparent rate constants of 0.0409 $min^{-1}$. The $k$ values of all the composites were higher than those of pure CCN and $Bi_{12}O_{17}Cl_2$. Figure S4 exhibits the photocatalytic degradation activity of TC by bulk CN, CCN, bulk $CN/Bi_{12}O_{17}Cl_2$, and $CCN/Bi_{12}O_{17}Cl_2$ under visible-light irradiation. Obviously, the CCN and $CCN/Bi_{12}O_{17}Cl_2$ showed higher activity than bulk CN and bulk $CN/Bi_{12}O_{17}Cl_2$, respectively. As can be seen in Table S3, the specific surface area of CCN was 179.03 $m^2 g^{-1}$, which was about 13 times that of the bulk CN (13.55 $m^2 g^{-1}$). Thus, CCN could provide more active sites for photocatalytic reaction, leading to the enhanced photocatalytic activity.

Effects of initial TC concentration (5, 10, 20, 30, and 40 mg $L^{-1}$) on the photocatalyst activities were investigated (Figure 7b). It was found that the removal efficiency dropped by increasing the initial TC concentration. The efficiency declined from 94% to 77% in 1 h oy irradiation, while the concentration of TC increased from 5 to 40 mg $L^{-1}$. It can be said that a higher concentration of TC could decrease the photogeneration of the reactive oxygen species and lead to fewer photons arriving at the surface of the photocatalyst. The result suggested that lower TC concentration was suitable to obtain the higher removal efficiency.

The stability of $CCN/Bi_{12}O_{17}Cl_2$ was also evaluated. As presented in Figure S5, after four cycles, the photocatalytic activity of $CCN/Bi_{12}O_{17}Cl_2$ exhibited no obvious reduction, indicating the good stability of $CCN/Bi_{12}O_{17}Cl_2$. Furthermore, the chemical stability of the fresh and used samples was further characterized by FT-IR, XRD, XPS, and SEM. As shown in

Figures S6 and S7, no noticeable alternations in the crystal, compositional, surface structure, and morphology are observed. Therefore, it can be said that the $CCN/Bi_{12}O_{17}Cl_2$ has excellent photocatalytic activity and good stability in the photocatalytic degradation of pollutants.

TC has autofluorescence because of its rigid structure,[67] and 3D excitation−emission spectra (EEMs) were used to further explore the degradation and mineralization properties of as-prepared $CCN/Bi_{12}O_{17}Cl_2$ (Figure 8). According to previous
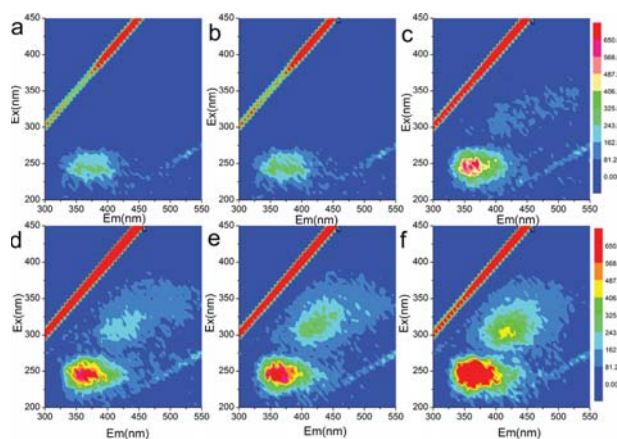
**Figure 8.** Three-dimensional EEMs of the aqueous solution: taken from the original solution (a), collected after 60 min adsorption in dark (b), and obtained after an irradiation time of 30, 60, 80, and 120 min (c−f), respectively.

studies, if TC began decomposition, then the humic acid peak in $\lambda_{ex}/\lambda_{em} = (305−330\ nm)/(430−450\ nm)$ and the fulvic acids peak in $\lambda_{ex}/\lambda_{em} = (240−250\ nm)/(435−450\ nm)$ would appear. No fluorescence was observed in Figure 8a,b, which indicated that TC was stable in the process of adsorption. The intensity of fluorescence increased from 30 to 60 min (Figure 8c−e). When the time reaches 120 min, the fluorescence decreased obviously, indicating that the low-molecular organic acid has been degraded (Figure 8f). This result also suggests that the $CCN/Bi_{12}O_{17}Cl_2$ exhibited high mineralization ability to TC. Degradation products have been identified using high-performance liquid−mass spectrometry (HPLC−MS). MS spectra of the TC and possible intermediate at a different reaction time have been added in Figure S8. Specifically, the tetracycline (TC) molecular with $m/z$ of 445.15 was first attacked by the holes or •OH to form its hydroxylated product ($m/z$ of 461.15). After that, the carbon chain of the hydroxylated product was split into the product ions at $m/z$ of 358.10. When the reactions progressed, the product ($m/z$ of 358.10) was further oxidized and ring-opened, which led to the generation of intermediate compounds with $m/z$ of 278.12, and 241.13. These ring-opening products were finally oxidized into $CO_2$ and $H_2O$. A suggested degradation pathway has been proposed in Figure S9.

**Possible Degradation Mechanism.** For elucidation of the reactive radicals of the 20% $CCN/Bi_{12}O_{17}Cl_2$ on the degradation of TC during the photocatalytic process, the active species trapping experiment was systematically investigated by using isopropanol (IPA), benzoquinone (BQ), and EDTA-2Na, which act as effective •OH, $O_2^{•−}$, and hole scavengers, respectively. The activity of $CCN/Bi_{12}O_{17}Cl_2$ causes a dramatic change by the addition of BQ and EDTA-2Na, suggesting that

$O_2^{•−}$ and holes are the two main oxidative radicals (Figure 9a,b). However, the activity of $CCN/Bi_{12}O_{17}Cl_2$ has been
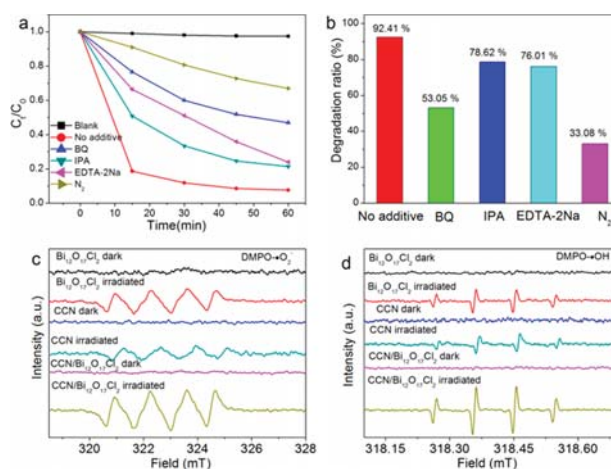
**Figure 9.** (a, b) Photocatalytic activities of the $CCN/Bi_{12}O_{17}Cl_2$ for degradation of TC under visible-light irradiation in the presence of trapping systems. ESR spectra of $Bi_{12}O_{17}Cl_2$ and $CCN/Bi_{12}O_{17}Cl_2$ dispersion under both the dark and visible-light irradiation (>420 nm) conditions: in methanol dispersion for $DMPO−O_2^{•−}$ (c), and in aqueous dispersion for $DMPO−•OH$ (d).

slightly changed with the addition of IPA, suggesting that the •OH radical played an assistant role in the degradation of TC over photocatalyst. For a study of the role of dissolved oxygen in the degradation process, the $CCN/Bi_{12}O_{17}Cl_2$ activities were tested in air and $N_2$ saturated suspensions. The rate of degradation was decreased from 94% to 33% in the $N_2$ saturation. More dissolved oxygen was beneficial to the process of photocatalytic degradation, which indicated that oxygen is a necessary medium in forming the superoxide free radical. These results agree with the above reactive radical test.

The above obtained results were further confirmed by ESR spin-trap measurements which were performed for identifying reactive radicals of CCN, $Bi_{12}O_{17}Cl_2$, and $CCN/Bi_{12}O_{17}Cl_2$. DMPO (5,5-dimethyl-pyrroline N-oxide) was employed as a spin trap to capture •OH and $O_2^{•−}$. As shown in Figure 9c,d, no ESR signal of the samples was detected in blank condition. In Figure 9c, upon visible-light irradiation for 8 min, a stronger signal was produced in $CCN/Bi_{12}O_{17}Cl_2$ than in $Bi_{12}O_{17}Cl_2$ and CCN, suggesting that more $O_2^{•−}$ was generated under irradiation. Meanwhile, in Figure 9d, a four-line spectrum with 1:2:2:1 was observed obviously in $CCN/Bi_{12}O_{17}Cl_2$, which were identified as the characteristic peaks of •OH. The peak of •OH in $Bi_{12}O_{17}Cl_2$ was also detected, but it was weaker than that in $CCN/Bi_{12}O_{17}Cl_2$. The results of ESR analysis are consistent with the radical trap experiments.

For further study of the mechanisms of photogenerated carriers, the conduction band (CB) and valence band (VB) positions of CCN and $Bi_{12}O_{17}Cl_2$ should be confirmed.[51,68] Mott−Schottky plots were utilized to calculate the flat band potential of CCN and $Bi_{12}O_{17}Cl_2$ at frequency of 1000 Hz (Figure 10a). The flat band potential of CCN was calculated to be −0.47 V, and that of $Bi_{12}O_{17}Cl_2$ was −0.44 V, versus Ag/AgCl electrode (SCE). Thus, they were −0.27 and −0.24 V versus normal hydrogen electrode (NHE).[52,65,69,70] In addition, the VB-XPS spectra of CCN and $Bi_{12}O_{17}Cl_2$ are shown in Figure 10b. For CCN and $Bi_{12}O_{17}Cl_2$, it can be seen that the
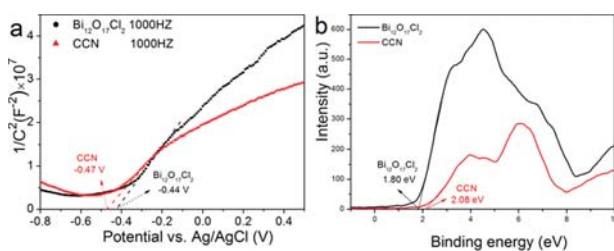
**Figure 10.** (a) Mott−Schottky plots of pure CCN and $Bi_{12}O_{17}Cl_2$ film electrodes at frequencies of 1000 Hz in an aqueous solution of $Na_2SO_4$ (0.1 M). (b) Valence band XPS spectra of pure CCN and $Bi_{12}O_{17}Cl_2$.

value between the Fermi level and VB were 2.08 and 1.80 eV, respectively. It is known that the flat potential was equal to the Fermi level for the n-type semiconductor. Then, the VB positions of CCN and $Bi_{12}O_{17}Cl_2$ were 1.81 and 1.56 eV, respectively. As a result, their band gaps were 2.21 and 2.33 eV, respectively (Figure 5b). Consequently, the CB positions of $Bi_{12}O_{17}Cl_2$ and CCN were −0.77 and −0.40 eV, respectively.

In general, the mechanism of CCN/$Bi_{12}O_{17}Cl_2$ composites on TC degradation is shown in Figure 11. $Bi_{12}O_{17}Cl_2$ and CCN
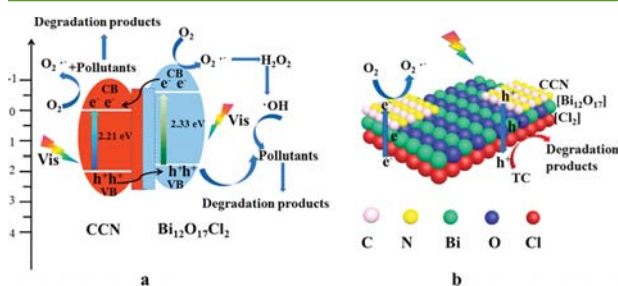


**Figure 11.** (a, b) Proposed charge separation process in the CCN/$Bi_{12}O_{17}Cl_2$ heterostructures under visible-light irradiation.

can be excited and generate the electrons and holes under light irradiation (Figure 11a). The electrons of $Bi_{12}O_{17}Cl_2$ can be transferred to the CCN because the CB potential of the $Bi_{12}O_{17}Cl_2$ is negative as compared to that of the CCN. Simultaneously, holes could be concentrated on the VB of the $Bi_{12}O_{17}Cl_2$. The $O_2$ captures the electrons to form the $O_2^{\bullet-}$. Then, $H^+$ reacted with $O_2^{\bullet-}$ and produced $H_2O_2$. The $H_2O_2$ was further reacted with electrons and generated $\bullet OH$ radicals.[30,71] The reactive radicals like $\bullet OH$ and $O_2^{\bullet-}$ could coefficiently oxidize the pollutant under visible-light irradiation. Also, the holes on the VB of the $Bi_{12}O_{17}Cl_2$ could degrade the pollutant directly. A proposed mechanism of charge separation on CCN/$Bi_{12}O_{17}Cl_2$ is presented in Figure 11b. For pristine $Bi_{12}O_{17}Cl_2$, the photogenerated carriers will recombine. The charge density of the $Bi_{12}O_{17}$ layer was greater than that of the $Cl_2$ layer, which can cause atom polarization to form an internal electric field.[40,70] The interaction between CCN and $Bi_{12}O_{17}Cl_2$ enhanced the transfer of internal electric field, which is beneficial for improving the photocatalytic activity of CCN/$Bi_{12}O_{17}Cl_2$ composites.

## CONCLUSIONS

In summary, novel CCN/$Bi_{12}O_{17}Cl_2$ photocatalysts were prepared via the ultrasonic chemical method. The CCN/$Bi_{12}O_{17}Cl_2$ composites exhibited outstanding photocatalytic degradation activities for TC. The activity of the 20% CCN/

$Bi_{12}O_{17}Cl_2$ sample is approximately 2.9, 1.5, and 32.1 times higher than those of pristine $Bi_{12}O_{17}Cl_2$, CCN, and BiOCl, respectively. The enhanced activity could be ascribed to the electrostatic interaction between CCN and $Bi_{12}O_{17}Cl_2$. The electrochemical results indicated that CCN/$Bi_{12}O_{17}Cl_2$ composite exhibited a superior charge transport property. Three-dimensional EEMs indicated that the CCN/$Bi_{12}O_{17}Cl_2$ composite has a high mineralization ability to TC. Moreover, the $O_2^{\bullet-}$, $h^+$, and $\bullet OH$ radicals in the CCN/$Bi_{12}O_{17}Cl_2$ catalytic system were validated. It can be seen that this study might provide a facile way for constructing highly efficient photocatalysts. Furthermore, the CCN/$Bi_{12}O_{17}Cl_2$ composite can be used in other refractory pollutant degradation and environmental remediation applications.

## ASSOCIATED CONTENT

### Ⓢ Supporting Information

The Supporting Information is available free of charge on the ACS Publications website at DOI: 10.1021/acssuschemeng.8b00782.

XRD, XPS, and FT-IR of the prepared samples and used samples, photocatalytic degradation, cycle runs, and HPLC−MS of TC by samples (PDF)

## AUTHOR INFORMATION

### Corresponding Authors

*E-mail: zgming@hnu.edu.cn. Phone:+86-731-88822754.
*E-mail: huangdanlian@hnu.edu.cn. Phone: +86-731-88823701.

### ORCID

Guangming Zeng: 0000-0002-4230-7647
Danlian Huang: 0000-0003-4955-5755

### Author Contributions

†C. Zhou, C. Lai, and P. Xu contributed equally to this article.

### Notes

The authors declare no competing financial interest.

## REFERENCES

(1) Zhang, Y.; Zeng, G.-M.; Tang, L.; Huang, D.-L.; Jiang, X.-Y.; Chen, Y.-N. A hydroquinone biosensor using modified core−shell magnetic nanoparticles supported on carbon paste electrode. *Biosens. Bioelectron.* **2007**, *22* (9−10), 2121−2126.

(2) Zhang, C.; Lai, C.; Zeng, G.; Huang, D.; Tang, L.; Yang, C.; Zhou, Y.; Qin, L.; Cheng, M. Nanoporous Au-based chronocoulometric aptasensor for amplified detection of $Pb^{2+}$ using DNAzyme modified with Au nanoparticles. *Biosens. Bioelectron.* **2016**, *81*, 61−67.

(3) Wu, H.; Lai, C.; Zeng, G.; Liang, J.; Chen, J.; Xu, J.; Dai, J.; Li, X.; Liu, J.; Chen, M. The interactions of composting and biochar and their implications for soil amendment and pollution remediation: a review. *Crit. Rev. Biotechnol.* **2017**, *37* (6), 754−764.

(4) Zhang, Y.; Zeng, G. M.; Tang, L.; Chen, J.; Zhu, Y.; He, X. X.; He, Y. Electrochemical sensor based on electrodeposited graphene-Au modified electrode and nanoAu carrier amplified signal strategy for attomolar mercury detection. *Anal. Chem.* **2015**, *87* (2), 989−996.

(5) Wan, J.; Zeng, G.; Huang, D.; Hu, L.; Xu, P.; Huang, C.; Deng, R.; Xue, W.; Lai, C.; Zhou, C. Rhamnolipid stabilized nano-chlorapatite: Synthesis and enhancement effect on Pb-and Cd-immobilization in polluted sediment. *J. Hazard. Mater.* **2018**, *343*, 332−339.

(6) Hu, L.; Wan, J.; Zeng, G.; Chen, A.; Chen, G.; Huang, Z.; He, K.; Cheng, M.; Zhou, C.; Xiong, W. Comprehensive evaluation of the cytotoxicity of CdSe/ZnS quantum dots in Phanerochaete chrys-osporium by cellular uptake and oxidative stress. *Environ. Sci.: Nano* **2017**, *4* (10), 2018−2029.

(7) Lai, C.; Wang, M.-M.; Zeng, G.-M.; Liu, Y.-G.; Huang, D.-L.; Zhang, C.; Wang, R.-Z.; Xu, P.; Cheng, M.; Huang, C. Synthesis of surface molecular imprinted TiO$_2$/graphene photocatalyst and its highly efficient photocatalytic degradation of target pollutant under visible light irradiation. *Appl. Surf. Sci.* **2016**, *390*, 368−376.

(8) Ren, X.; Zeng, G.; Tang, L.; Wang, J.; Wan, J.; Liu, Y.; Yu, J.; Yi, H.; Ye, S.; Deng, R. Sorption, transport and biodegradation−an insight into bioavailability of persistent organic pollutants in soil. *Sci. Total Environ.* **2018**, *610*, 1154−1163.

(9) Xiong, W.; Tong, J.; Yang, Z.; Zeng, G.; Zhou, Y.; Wang, D.; Song, P.; Xu, R.; Zhang, C.; Cheng, M. Adsorption of phosphate from aqueous solution using iron-zirconium modified activated carbon nanofiber: Performance and mechanism. *J. Colloid Interface Sci.* **2017**, *493*, 17−23.

(10) Schlienger, S.; Alauzun, J.; Michaux, F.; Vidal, L.; Parmentier, J.; Gervais, C.; Babonneau, F.; Bernard, S.; Miele, P.; Parra, J. Micro-, mesoporous boron nitride-based materials templated from zeolites. *Chem. Mater.* **2012**, *24* (1), 88−96.

(11) Cheng, M.; Zeng, G.; Huang, D.; Lai, C.; Xu, P.; Zhang, C.; Liu, Y. Hydroxyl radicals based advanced oxidation processes (AOPs) for remediation of soils contaminated with organic compounds: A review. *Chem. Eng. J.* **2016**, *284*, 582−598.

(12) Xu, P.; Zeng, G. M.; Huang, D. L.; Feng, C. L.; Hu, S.; Zhao, M. H.; Lai, C.; Wei, Z.; Huang, C.; Xie, G. X.; Liu, Z. F. Use of iron oxide nanomaterials in wastewater treatment: A review. *Sci. Total Environ.* **2012**, *424*, 1−10.

(13) Zhang, C.; Lai, C.; Zeng, G.; Huang, D.; Yang, C.; Wang, Y.; Zhou, Y.; Cheng, M. Efficacy of carbonaceous nanocomposites for sorbing ionizable antibiotic sulfamethazine from aqueous solution. *Water Res.* **2016**, *95*, 103−112.

(14) Shao, H.; Zhao, X.; Wang, Y.; Mao, R.; Wang, Y.; Qiao, M.; Zhao, S.; Zhu, Y. Synergetic activation of peroxymonosulfate by Co$_3$O$_4$ modified g-C$_3$N$_4$ for enhanced degradation of diclofenac sodium under visible light irradiation. *Appl. Catal., B* **2017**, *218*, 810−818.

(15) Huang, D.; Hu, C.; Zeng, G.; Cheng, M.; Xu, P.; Gong, X.; Wang, R.; Xue, W. Combination of Fenton processes and biotreat-ment for wastewater treatment and soil remediation. *Sci. Total Environ.* **2017**, *574*, 1599−1610.

(16) Yang, C.; Chen, H.; Zeng, G.; Yu, G.; Luo, S. Biomass accumulation and control strategies in gas biofiltration. *Biotechnol. Adv.* **2010**, *28* (4), 531−540.

(17) Huang, D.-L.; Zeng, G.-M.; Feng, C.-L.; Hu, S.; Jiang, X.-Y.; Tang, L.; Su, F.-F.; Zhang, Y.; Zeng, W.; Liu, H.-L. Degradation of lead-contaminated lignocellulosic waste by Phanerochaete chrysospo-rium and the reduction of lead toxicity. *Environ. Sci. Technol.* **2008**, *42* (13), 4946−4951.

(18) Zhu, H.; Chen, D.; Li, N.; Xu, Q.; Li, H.; He, J.; Lu, J. Graphene Foam with Switchable Oil Wettability for Oil and Organic Solvents Recovery. *Adv. Funct. Mater.* **2015**, *25* (4), 597−605.

(19) Zhong, S.; Zhou, C.; Zhang, X.; Zhou, H.; Li, H.; Zhu, X.; Wang, Y. A novel molecularly imprinted material based on magnetic halloysite nanotubes for rapid enrichment of 2, 4-dichlorophenoxy-acetic acid in water. *J. Hazard. Mater.* **2014**, *276*, 58−65.

(20) Huang, D.; Xue, W.; Zeng, G.; Wan, J.; Chen, G.; Huang, C.; Zhang, C.; Cheng, M.; Xu, P. Immobilization of Cd in river sediments by sodium alginate modified nanoscale zero-valent iron: Impact on enzyme activities and microbial community diversity. *Water Res.* **2016**, *106*, 15−25.

(21) Huang, D.-L.; Wang, R.-Z.; Liu, Y.-G.; Zeng, G.-M.; Lai, C.; Xu, P.; Lu, B.-A.; Xu, J.-J.; Wang, C.; Huang, C. Application of molecularly imprinted polymers in wastewater treatment: a review. *Environ. Sci. Pollut. Res.* **2015**, *22* (2), 963−977.

(22) Cheng, M.; Zeng, G.; Huang, D.; Lai, C.; Liu, Y.; Zhang, C.; Wan, J.; Hu, L.; Zhou, C.; Xiong, W. Efficient degradation of sulfamethazine in simulated and real wastewater at slightly basic pH values using Co-SAM-SCS/H$_2$O$_2$ Fenton-like system. *Water Res.* **2018**, *138*, 7−18.

(23) Huang, D.; Liu, L.; Zeng, G.; Xu, P.; Huang, C.; Deng, L.; Wang, R.; Wan, J. The effects of rice straw biochar on indigenous microbial community and enzymes activity in heavy metal-contaminated sediment. *Chemosphere* **2017**, *174*, 545−553.

(24) Wang, J.; Yang, Z.; Gao, X.; Yao, W.; Wei, W.; Chen, X.; Zong, R.; Zhu, Y. Core-shell g-C 3 N 4 @ZnO composites as photoanodes with double synergistic effects for enhanced visible-light photo-electrocatalytic activities. *Appl. Catal., B* **2017**, *217*, 169−180.

(25) Yang, S.; Chen, D.; Li, N.; Xu, Q.; Li, H.; He, J.; Lu, J. Surface-Nanoengineered Bacteria for Efficient Local Enrichment and Biodegradation of Aqueous Organic Wastes: Using Phenol as a Model Compound. *Adv. Mater.* **2016**, *28* (15), 2916−2922.

(26) Zhou, C.; Li, H.; Zhou, H.; Wang, H.; Yang, P.; Zhong, S. Water - compatible halloysite - imprinted polymer by Pickering emulsion polymerization for the selective recognition of herbicides. *J. sep. sci.* **2015**, *38* (8), 1365−1371.

(27) Gong, J.-L.; Wang, B.; Zeng, G.-M.; Yang, C.-P.; Niu, C.-G.; Niu, Q.-Y.; Zhou, W.-J.; Liang, Y. Removal of cationic dyes from aqueous solution using magnetic multi-wall carbon nanotube nano-composite as adsorbent. *J. Hazard. Mater.* **2009**, *164* (2−3), 1517−1522.

(28) Cheng, Y.; He, H.; Yang, C.; Zeng, G.; Li, X.; Chen, H.; Yu, G. Challenges and solutions for biofiltration of hydrophobic volatile organic compounds. *Biotechnol. Adv.* **2016**, *34* (6), 1091−1102.

(29) Gong, X.; Huang, D.; Liu, Y.; Zeng, G.; Wang, R.; Wan, J.; Zhang, C.; Cheng, M.; Qin, X.; Xue, W. Stabilized Nanoscale Zerovalent Iron Mediated Cadmium Accumulation and Oxidative Damage of Boehmeria nivea (L.) Gaudich Cultivated in Cadmium Contaminated Sediments. *Environ. Sci. Technol.* **2017**, *51* (19), 11308−11316.

(30) Pan, M.; Zhang, H.; Gao, G.; Liu, L.; Chen, W. Facet-dependent catalytic activity of nanosheet-assembled bismuth oxyiodide micro-spheres in degradation of bisphenol A. *Environ. Sci. Technol.* **2015**, *49* (10), 6240−6248.

(31) Li, K.; Han, M.; Chen, R.; Li, S.-L.; Xie, S.-L.; Mao, C.; Bu, X.; Cao, X.-L.; Dong, L.-Z.; Feng, P.; Lan, Y.-Q. Hexagonal@Cubic CdS Core@Shell Nanorod Photocatalyst for Highly Active Production of H$_2$ with Unprecedented Stability. *Adv. Mater.* **2016**, *28* (40), 8906−8911.

(32) Li, J.; Wu, X.; Pan, W.; Zhang, G.; Chen, H. Vacancy-Rich Monolayer BiO2−x as a Highly Efficient UV, Visible, and Near-Infrared Responsive Photocatalyst. *Angew. Chem.* **2018**, *130* (2), 500−504.

(33) Li, H.; Shi, J.; Zhao, K.; Zhang, L. Sustainable molecular oxygen activation with oxygen vacancies on the {001} facets of BiOCl nanosheets under solar light. *Nanoscale* **2014**, *6* (23), 14168−14173.

(34) Li, J.; Li, H.; Zhan, G.; Zhang, L. Solar Water Splitting and Nitrogen Fixation with Layered Bismuth Oxyhalides. *Acc. Chem. Res.* **2017**, *50* (1), 112−121.

(35) Wang, C.-Y.; Zhang, X.; Qiu, H.-B.; Wang, W.-K.; Huang, G.-X.; Jiang, J.; Yu, H.-Q. Photocatalytic degradation of bisphenol A by oxygen-rich and highly visible-light responsive Bi12O17Cl2 nanobelts. *Appl. Catal., B* **2017**, *200*, 659−665.

(36) Xiao, X.; Jiang, J.; Zhang, L. Selective oxidation of benzyl alcohol into benzaldehyde over semiconductors under visible light: The case of Bi$_{12}$O$_{17}$Cl$_2$ nanobelts. *Appl. Catal., B* **2013**, *142*, 487−493.

(37) Huang, H.; Xiao, K.; He, Y.; Zhang, T.; Dong, F.; Du, X.; Zhang, Y. In situ assembly of BiOI@Bi$_{12}$O$_{17}$Cl$_2$ p−n junction: charge induced unique front-lateral surfaces coupling heterostructure with high exposure of BiOI {001} active facets for robust and nonselective photocatalysis. *Appl. Catal., B* 2016, *199*, 75−86.

(38) He, G.; Xing, C.; Xiao, X.; Hu, R.; Zuo, X.; Nan, J. Facile synthesis of flower-like Bi$_{12}$O$_{17}$Cl$_2$/β-Bi$_2$O$_3$ composites with enhanced visible light photocatalytic performance for the degradation of 4-tert-butylphenol. *Appl. Catal., B* 2015, *170−171*, 1−9.

(39) Hao, L.; Huang, H.; Guo, Y.; Du, X.; Zhang, Y. Bismuth oxychloride homogeneous phasejunction BiOCl/Bi$_{12}$O$_{17}$Cl$_2$ with unselectively efficient photocatalytic activity and mechanism insight. *Appl. Surf. Sci.* 2017, *420*, 303−312.

(40) Li, J.; Zhan, G.; Yu, Y.; Zhang, L. Superior visible light hydrogen evolution of Janus bilayer junctions via atomic-level charge flow steering. *Nat. Commun.* 2016, *7*, 11480.

(41) Yang, P.; Ou, H.; Fang, Y.; Wang, X. A Facile Steam Reforming Strategy to Delaminate Layered Carbon Nitride Semiconductors for Photoredox Catalysis. *Angew. Chem., Int. Ed.* 2017, *56* (14), 3992−3996.

(42) Zheng, D.; Cao, X.-N.; Wang, X. Precise Formation of a Hollow Carbon Nitride Structure with a Janus Surface To Promote Water Splitting by Photoredox Catalysis. *Angew. Chem., Int. Ed.* 2016, *55* (38), 11512−11516.

(43) Lin, L.; Ou, H.; Zhang, Y.; Wang, X. Tri-s-triazine-Based Crystalline Graphitic Carbon Nitrides for Highly Efficient Hydrogen Evolution Photocatalysis. *ACS Catal.* 2016, *6* (6), 3921−3931.

(44) Huang, D.; Wang, X.; Zhang, C.; Zeng, G.; Peng, Z.; Zhou, J.; Cheng, M.; Wang, R.; Hu, Z.; Qin, X. Sorptive removal of ionizable antibiotic sulfamethazine from aqueous solution by graphene oxide-coated biochar nanocomposites: Influencing factors and mechanism. *Chemosphere* 2017, *186*, 414−421.

(45) Deng, Y.; Tang, L.; Zeng, G.; Zhu, Z.; Yan, M.; Zhou, Y.; Wang, J.; Liu, Y.; Wang, J. Insight into highly efficient simultaneous photocatalytic removal of Cr(VI) and 2,4-diclorophenol under visible light irradiation by phosphorus doped porous ultrathin g-C$_3$N$_4$ nanosheets from aqueous media: Performance and reaction mechanism. *Appl. Catal., B* 2017, *203*, 343−354.

(46) Zheng, Y.; Lin, L. H.; Wang, B.; Wang, X. C. Graphitic Carbon Nitride Polymers toward Sustainable Photoredox Catalysis. *Angew. Chem., Int. Ed.* 2015, *54* (44), 12868−12884.

(47) Wan, Z.; Zhang, G.; Wu, X.; Yin, S. Novel visible-light-driven Z-scheme Bi$_{12}$GeO$_{20}$/g-C$_3$N$_4$ photocatalyst: Oxygen-induced pathway of organic pollutants degradation and proton assisted electron transfer mechanism of Cr(VI) reduction. *Appl. Catal., B* 2017, *207*, 17−26.

(48) Yang, S.-F.; Niu, C.-G.; Huang, D.-W.; Zhang, H.; Liang, C.; Zeng, G.-M. SrTiO$_3$ nanocubes decorated with Ag/AgCl nanoparticles as photocatalysts with enhanced visible-light photocatalytic activity towards the degradation of dyes, phenol and bisphenol A. *Environ. Sci.: Nano* 2017, *4* (3), 585−595.

(49) Wang, K.; Zhang, G.; Li, J.; Li, Y.; Wu, X. 0D/2D Z-Scheme Heterojunctions of Bismuth Tantalate Quantum Dots/Ultrathin g-C3N4 Nanosheets for Highly Efficient Visible Light Photocatalytic Degradation of Antibiotics. *ACS Appl. Mater. Interfaces* 2017, *9* (50), 43704−43715.

(50) Wei, Z.; Liang, F.; Liu, Y.; Luo, W.; Wang, J.; Yao, W.; Zhu, Y. Photoelectrocatalytic degradation of phenol-containing wastewater by TiO$_2$/g-C$_3$N$_4$ hybrid heterostructure thin film. *Appl. Catal., B* 2017, *201*, 600−606.

(51) Jiang, G.; Li, X.; Lan, M.; Shen, T.; Lv, X.; Dong, F.; Zhang, S. Monodisperse bismuth nanoparticles decorated graphitic carbon nitride: Enhanced visible-light-response photocatalytic NO removal and reaction pathway. *Appl. Catal., B* 2017, *205*, 532−540.

(52) Tian, N.; Zhang, Y.; Li, X.; Xiao, K.; Du, X.; Dong, F.; Waterhouse, G. I. N.; Zhang, T.; Huang, H. Precursor-reforming protocol to 3D mesoporous g-C$_3$N$_4$ established by ultrathin self-doped nanosheets for superior hydrogen evolution. *Nano Energy* 2017, *38*, 72−81.

(53) Dang, K.; Wang, T.; Li, C.; Zhang, J.; Liu, S.; Gong, J. Improved Oxygen Evolution Kinetics and Surface States Passivation of Ni-Bi Co-Catalyst for a Hematite Photoanode. *Engineering* 2017, *3* (3), 285−289.

(54) Chen, F.; Yang, Q.; Wang, Y.; Zhao, J.; Wang, D.; Li, X.; Guo, Z.; Wang, H.; Deng, Y.; Niu, C.; Zeng, G. Novel ternary heterojunction photcocatalyst of Ag nanoparticles and g-C$_3$N$_4$ nanosheets co-modified BiVO$_4$ for wider spectrum visible-light photocatalytic degradation of refractory pollutant. *Appl. Catal., B* 2017, *205*, 133−147.

(55) Chen, F.; Yang, Q.; Wang, S.; Yao, F.; Sun, J.; Wang, Y.; Zhang, C.; Li, X.; Niu, C.; Wang, D.; Zeng, G. Graphene oxide and carbon nitride nanosheets co-modified silver chromate nanoparticles with enhanced visible-light photoactivity and anti-photocorrosion properties towards multiple refractory pollutants degradation. *Appl. Catal., B* 2017, *209*, 493−505.

(56) Zhang, J.; Wang, T.; Chang, X.; Li, A.; Gong, J. Fabrication of porous nanoflake BiMO x (M= W, V, and Mo) photoanodes via hydrothermal anion exchange. *Chem. Sci.* 2016, *7* (10), 6381−6386.

(57) Wang, R.; Pan, K.; Han, D.; Jiang, J.; Xiang, C.; Huang, Z.; Zhang, L.; Xiang, X. Solar - Driven H2O2 Generation From H$_2$O and O$_2$ Using Earth - Abundant Mixed - Metal Oxide@ Carbon Nitride Photocatalysts. *ChemSusChem* 2016, *9* (17), 2470−2479.

(58) Wang, R.; Zhang, X.; Li, F.; Cao, D.; Pu, M.; Han, D.; Yang, J.; Xiang, X. Energy-level dependent H$_2$O$_2$ production on metal-free, carbon-content tunable carbon nitride photocatalysts. *J. Energy Chem.* 2018, *27* (2), 343−350.

(59) Zhou, C. Y.; Lai, C.; Huang, D. L.; Zeng, G. M.; Zhang, C.; Cheng, M.; Hu, L.; Wan, J.; Xiong, W. P.; Wen, M.; Wen, X. F.; Qin, L. Highly porous carbon nitride by supramolecular preassembly of monomers for photocatalytic removal of sulfamethazine under visible light driven. *Appl. Catal., B* 2018, *220*, 202−210.

(60) Wang, C.-Y.; Zhang, X.; Song, X.-N.; Wang, W.-K.; Yu, H.-Q. Novel Bi$_{12}$O$_{15}$Cl$_6$ Photocatalyst for the Degradation of Bisphenol A under Visible-Light Irradiation. *ACS Appl. Mater. Interfaces* 2016, *8* (8), 5320−5326.

(61) Zhou, C.; Lai, C.; Xu, P.; Zeng, G.; Huang, D.; Zhang, C.; Cheng, M.; Hu, L.; Wan, J.; Liu, Y.; Xiong, W.; Deng, Y.; Wen, M. In Situ Grown AgI/Bi$_{12}$O$_{17}$Cl$_2$ Heterojunction Photocatalysts for Visible Light Degradation of Sulfamethazine: Efficiency, Pathway, and Mechanism. *ACS Sustainable Chem. Eng.* 2018, *6* (3), 4174−4184.

(62) Shalom, M.; Inal, S.; Fettkenhauer, C.; Neher, D.; Antonietti, M. Improving Carbon Nitride Photocatalysis by Supramolecular Pre-organization of Monomers. *J. Am. Chem. Soc.* 2013, *135* (19), 7118−7121.

(63) Shao, H.; Zhao, X.; Wang, Y.; Mao, R.; Wang, Y.; Qiao, M.; Zhao, S.; Zhu, Y. Synergetic activation of peroxymonosulfate by Co$_3$O$_4$ modified g-C$_3$N$_4$ for enhanced degradation of diclofenac sodium under visible light irradiation. *Appl. Catal., B* 2017, *218*, 810−818.

(64) Zhang, M.; Luo, W.; Wei, Z.; Jiang, W.; Liu, D.; Zhu, Y. Separation free C$_3$N$_4$/SiO$_2$ hybrid hydrogels as high active photo-catalysts for TOC removal. *Appl. Catal., B* 2016, *194*, 105−110.

(65) Cui, W.; Li, J.; Dong, F.; Sun, Y.; Jiang, G.; Cen, W.; Lee, S. C.; Wu, Z. Highly efficient performance and conversion pathway of photocatalytic NO oxidation on SrO-clusters@ amorphous carbon nitride. *Environ. Sci. Technol.* 2017, *51* (18), 10682−10690.

(66) Tang, Y.; Wang, R.; Yang, Y.; Yan, D.; Xiang, X. Highly enhanced photoelectrochemical water oxidation efficiency based on triadic quantum dot/layered double hydroxide/BiVO$_4$ photoanodes. *ACS Appl. Mater. Interfaces* 2016, *8* (30), 19446−19455.

(67) Cheng, M.; Zeng, G.; Huang, D.; Lai, C.; Liu, Y.; Xu, P.; Zhang, C.; Wan, J.; Hu, L.; Xiong, W. Salicylic acid−methanol modified steel converter slag as heterogeneous Fenton-like catalyst for enhanced degradation of alachlor. *Chem. Eng. J.* 2017, *327*, 686−693.

(68) Cui, W.; Li, J.; Cen, W.; Sun, Y.; Lee, S.; Dong, F. Steering the interlayer energy barrier and charge flow via bioriented transportation channels in g-C$_3$N$_4$: Enhanced photocatalysis and reaction mechanism. *J. Catal.* 2017, *352*, 351−360.

(69) Xia, J.; Ji, M.; Di, J.; Wang, B.; Yin, S.; Zhang, Q.; He, M.; Li, H. Construction of ultrathin $C_3N_4/Bi_4O_5I_2$ layered nanojunctions via ionic liquid with enhanced photocatalytic performance and mechanism insight. *Appl. Catal., B* **2016**, *191*, 235−245.

(70) Bai, Y.; Ye, L.; Wang, L.; Shi, X.; Wang, P.; Bai, W.; Wong, P. K. $gC_3N_4/Bi_4O_5I_2$ heterojunction with $I_3^-/I^-$ redox mediator for enhanced photocatalytic $CO_2$ conversion. *Appl. Catal., B* **2016**, *194*, 98−104.

(71) Huang, Y.; Kang, S.; Yang, Y.; Qin, H.; Ni, Z.; Yang, S.; Li, X. Facile synthesis of $Bi/Bi_2WO_6$ nanocomposite with enhanced photocatalytic activity under visible light. *Appl. Catal., B* **2016**, *196*, 89−99.